

Emergent Chirality and Hyperuniformity in an Active Mixture with Nonreciprocal Interactions

Jianchao Chen¹, Xiaokang Lei^{2,3,*}, Yalun Xiang⁴, Mengyuan Duan³, Xingguang Peng^{4,†}, and H. P. Zhang^{1,‡}

¹*School of Physics and Astronomy, Institute of Natural Sciences and MOE-LSC, Shanghai Jiao Tong University, Shanghai, 200240, China*

²*Faculty of Electronic and Information Engineering, and MOE Key Lab for Intelligent Networks and Network Security, Xi'an Jiaotong University, Xi'an, 710049, China*

³*College of Information and Control Engineering, Xi'an University of Architecture and Technology, Xi'an, 710055, China*

⁴*School of Marine Science and Technology, Northwestern Polytechnical University, Xi'an, 710072, China*



(Received 16 September 2023; revised 21 December 2023; accepted 26 February 2024; published 14 March 2024)

We investigate collective dynamics in a binary mixture of programmable robots in experiments and simulations. While robots of the same species align their motion direction, interaction between species is distinctly nonreciprocal: species A aligns with B and species B antialigns with A. This nonreciprocal interaction gives rise to the emergence of collective chiral motion that can be stabilized by limiting the robot angular speed to be below a threshold. Within the chiral phase, increasing the robot density or extending the range of local repulsive interactions can drive the system through an absorbing-active transition. At the transition point, the robots exhibit a remarkable capacity for self-organization, forming disordered hyperuniform states.

DOI: [10.1103/PhysRevLett.132.118301](https://doi.org/10.1103/PhysRevLett.132.118301)

Newton's third law establishes that the interactions between particles are reciprocal. This is true not only for the fundamental microscopic forces but also for equilibrium effective forces, which are constrained by the detailed balance in thermal equilibrium [1]. However, an intriguing departure from this action-reaction symmetry arises when interactions are mediated through nonequilibrium environments [2,3]. Such nonreciprocal (NR) interactions are prevalent in active matter systems [4–13] where thermal equilibrium is broken at the individual level and particles often interact through actively generated hydrodynamic or chemical fields. Examples of NR interactions span a wide spectrum of active systems, from cell populations [14,15] to active colloids [16–21] and feedback-controlled robotic systems [22–27].

Extensive theoretical and numerical investigations have revealed that NR interactions can give rise to *time-dependent* collective states that profoundly reshape system dynamics [28–37]. For instance, the introduction of NR interactions into a Cahn-Hilliard model sets the phase-separated state into motion, resulting in traveling density waves [28–32]. An analogous phenomenon in angular dynamics is the formation of a collective chiral state in a two-species Vicsek model [38–40], where particles of both species exhibit coherent rotation in the same direction [33,41]. The emergence of these time-dependent collective states in NR systems exemplifies a class of transitions characterized by parity-time symmetry breaking [7,29,33,42], unleashing a diverse array of novel phenomena in phase separation and pattern formation [28–37].

While theoretical and numerical studies have shed much light on the origins, dynamics, and implications of time-dependent collective states [28–37], quantitative experiments in this area have been limited. This limitation stems, in part, from the inherent difficulty in precisely controlling NR interactions at the system level [14–20]. To address this challenge, we have developed an experimental system involving robots [22–27,33], whose interactions are programmed according to a standard NR two-species Vicsek model, augmented with an angular speed threshold and local repulsive interactions. Our experiments, together with analytical and numerical analysis, demonstrate that the angular speed threshold stabilizes chiral collective states over a broad parameter range. Increasing local repulsion drives robots within chiral states through an absorbing-active transition and the robots exhibit a disordered hyperuniform distribution at the transition.

Our experimental setup comprises $N = 48$ identical robots moving in a $5.4 \text{ m} \times 5 \text{ m}$ arena, depicted in Fig. 1(a). We track robot identity m , position \mathbf{r}_m , and heading θ_m via an optical motion capture system from NOKOV, which sends tracking data to a central server at a frequency of 300 Hz. The server computes robot angular velocity $\dot{\theta}_m$ from received data, according to a process detailed in the following section. Subsequently, the server broadcasts these computed angular velocities to all robots via a customized wireless serial communication protocol. These robots update their angular velocities to the broadcast values at a frequency of 5 Hz, and they all move with a

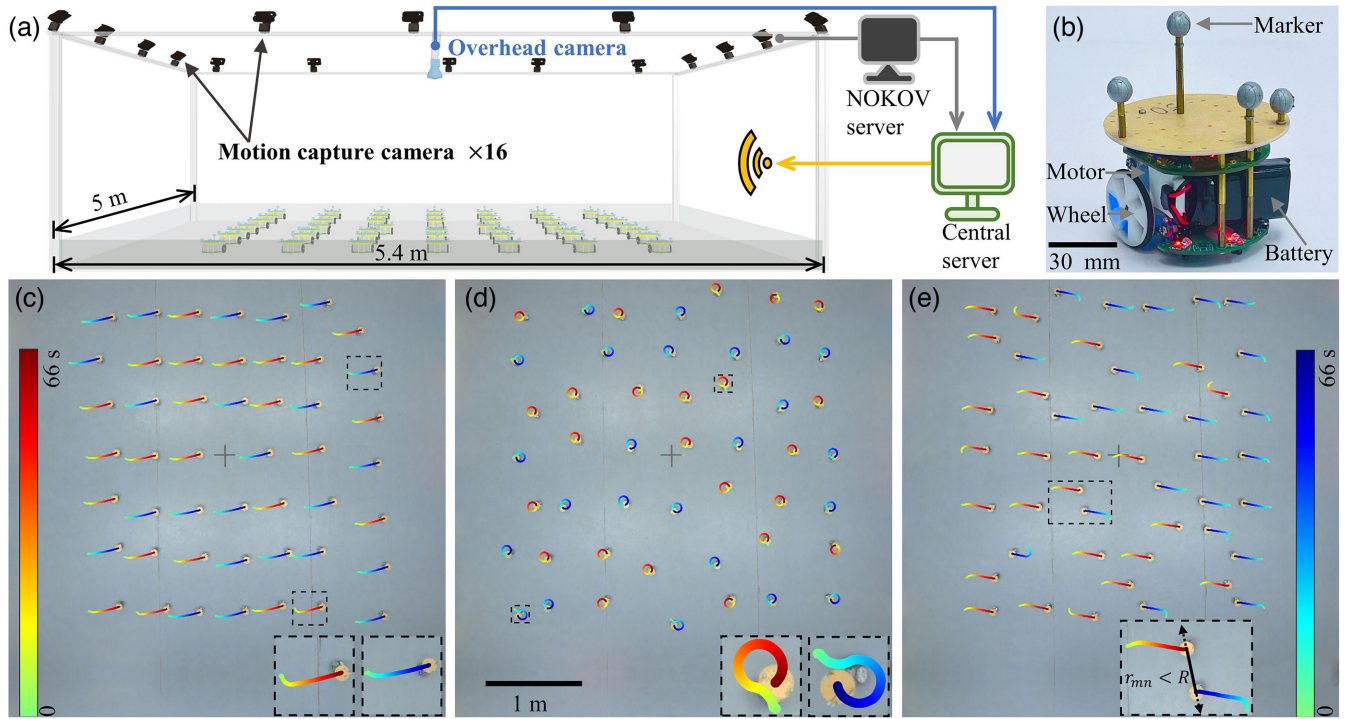


FIG. 1. Experimental setup and collective states. (a) An overview of the experimental setup, comprising robots in an arena, an overhead camera, a NOKOV system of 16 motion capture cameras, and a central computer [see Fig. S1(b) for a picture of the system [43]]. (b) A side-view picture of a robot. Formation of flocking (c), chiral (d), and antiflocking (e) states. Trajectories of the robots are color-coded based on time. Warm colors (on the left) represent species A, while cold colors (on the right) represent species B. Insets in (c)–(e) provide enlarged views of two trajectories indicated by black boxes. The inset of (e) shows that two robots experience local repulsion when their separation falls below the repulsion distance R . Experimental parameters include: $J_+ = 0.03$ rad/s (c), -0.02 rad/s (d), -0.04 rad/s (e), $J_- = 0.04$ rad/s, $J_{AA} = J_{BB} = 0.0175$ rad/s, $\Omega = 0.1$ rad/s, $R = 260$ mm, and $v_0 = 5$ mm/s. The normal reflection condition is applied at the arena boundaries. See Movies S1–S3 for system evolution over a longer period time [43].

constant speed v_0 :

$$\partial_t \mathbf{r}_m = v_0 (\cos(\theta_m) \hat{x} + \sin(\theta_m) \hat{y}). \quad (1)$$

To calculate the angular velocities $\dot{\theta}_m$, the central server aggregates the contributions from orientational interactions pertaining to the m th robot:

$$\omega_m = \sum_{n \neq m} J_{mn} \sin(\theta_n - \theta_m), \quad (2)$$

where we sum over all robot pairs and J_{mn} is the interaction constant. We categorize the N robots into two species, A and B, with equal numbers: $N_A = N_B = N/2$. Robots within the same species align their motion: $J_{AA} = J_{BB} > 0$. Interspecies interactions, which are of similar strength as J_{AA} and J_{BB} , may exhibit nonreciprocity: $J_{AB} \neq J_{BA}$. We define $J_+ = (J_{AB} + J_{BA})/2$ and $J_- = (J_{AB} - J_{BA})/2$ to quantify the strength of reciprocal and nonreciprocal interactions. We also incorporate local robot-robot repulsion to prevent robots from colliding. As shown in the inset of Fig. 1(e) and Sec. IV(A) in the Supplemental Material (SM) [43], two robots turn away from each other when their distance is smaller than R [44]. A similar

repulsion mechanism is implemented concerning the arena boundaries, preventing robots from exiting the arena. The full equation encompassing both orientational and repulsive interactions for computing ω_m is provided in Eq. (S7) [43]. Before sending the computed ω_m to robots, we apply an angular speed threshold Ω :

$$\dot{\theta}_m = \text{sgn}(\omega_m) \min(|\omega_m|, \Omega), \quad (3)$$

where $\text{sgn}()$ and $\min()$ are sign and minimum functions. This thresholding procedure, widely employed in prior numerical and experimental studies [45–47], accounts for the practical constraints on robot maneuverability.

In the initiation of our experiments, 48 robots are placed in the arena with randomized headings. To preclude any potential repulsive interactions, the robots are initially positioned at a considerable distance from both each other and the arena boundaries. As shown in Fig. S3(a), orientational interactions drive the system through a transient period with significant mean angular velocity. Then, the system reaches one of three distinctive states: flocking, antiflocking, and chiral states. We note that the steady flocking and antiflocking states can be disrupted by robot-robot or robot-boundary repulsion [48–50] and that only

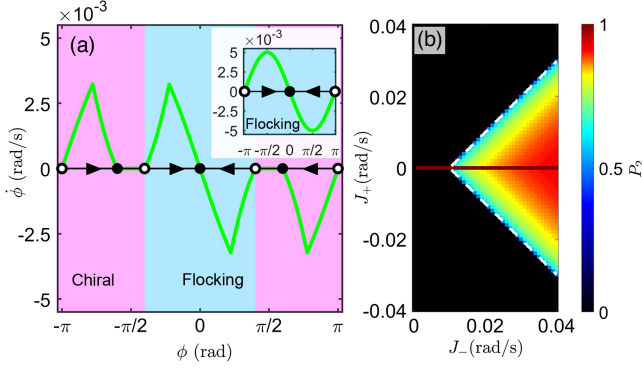


FIG. 2. Two-robot dynamics. (a) Rate change of heading difference $\dot{\phi}$ with (main panel) and without (inset) angular speed threshold. Stable and unstable fixed points are denoted by filled and empty circles on the x axis, respectively. The blue and magenta shades indicate the initial heading difference that leads to flocking and chiral states, respectively. (b) Probability of two robots to enter chiral phase from a random initial condition. Parameters include $J_{AB} = 0.0155$ rad/s, $J_{BA} = -0.0105$ rad/s in (a), and $\Omega = 0.01$ rad/s in (a),(b).

steady states before such disruptions are analyzed to obtain experimental results in Figs. 1 and 3. Beyond the temporal range considered above, robot-boundary interactions can play a decisive role in determining the long-time flocking and antiflocking dynamics, as shown in Figs. S4 and S5 [43].

In experiments, we vary J_{AB} and J_{BA} while keeping $J_- = 0.04$ rad/s. When $|J_+|$ is sufficiently large, the system enters time-invariant flocking states in Fig. 1(c) with $J_+ = 0.03$ rad/s, or antiflocking states in Fig. 1(e) with $J_+ = -0.04$ rad/s [33]. Conversely, if nonreciprocal interactions predominate, a time-dependent chiral state appears: all robots in Fig. 1(d) and Movie S2 eventually move in circles with an angular velocity at the threshold $\Omega = 0.1$ rad/s. We use robot headings to define two order parameters for each species and we have $\Lambda^\alpha e^{i\Phi^\alpha} = (1/N_\alpha) \sum_{m=1}^{N_\alpha} e^{i\theta_m^\alpha}$, where the amplitude Λ^α and the heading Φ^α characterize the heading coherence and the mean heading of the species α , respectively [51]. Mean amplitude $\Lambda = (\Lambda^A + \Lambda^B)/2$ in Fig. S3(b) shows that robots in three states are polarly aligned within each species. We also compute the difference between the mean headings: $\Phi = \Phi^A - \Phi^B$: Fig. S3(c) shows that Φ assumes values of 0 , π , and 0.55π for flocking, antiflocking, and chiral states, respectively.

Chiral states in our system are stable, a notable departure from transient chiral states observed in previous robotic experiments [33]. To elucidate the mechanisms underlying this stability, we consider the scenario involving two NR robots ($N = 2$) [33,41]. The heading difference of two robots, denoted as $\phi = \theta_A - \theta_B$, evolves according to the equation $\dot{\phi} = -2J_+ \sin(\phi)$. This equation exhibits stable fixed points at $\phi = 0$ if $J_+ > 0$ or $\phi = \pi$ if $J_+ < 0$

[see inset of Fig. 2(a)]. Consequently, in the absence of any angular speed threshold, the stable chiral motion of two robots can only be sustained under conditions of fully nonreciprocal interactions $J_+ = 0$. This partly explains why only transient chiral states were experimentally observed in Ref. [33].

The introduction of the threshold Ω in Eq. (3) qualitatively changes the scenario, as shown in the right panel of Movie S7, wherein both robots reach the threshold Ω and form a chiral state. Beyond this specific example, we plot the analytical solution of $\dot{\phi}$ with the threshold in Fig. 2(a), which shows new stable fixed points. Robots initialized within regions shaded in magenta ultimately evolve toward chiral states. This development allows us to compute the probability of two robots reaching a chiral state from random initial ϕ : $P_2 = 1 - \max[\text{asin}(\Omega/|J_{AB}|), \text{asin}(\Omega/|J_{BA}|)]/\pi$, where $\max[]$ is the maximum function. As shown in Fig. 2(b), the region of nonzero P_2 (excluding the case where $J_+ = 0$) is bounded on the left by two white lines defined as

$$J_+ = \pm[J_- - \Omega/(N/2)]. \quad (4)$$

On the right side of these lines, we have $J_{AB} J_{BA} < 0$ and $\Omega < \min(N|J_{AB}|/2, N|J_{BA}|/2)$. Under these conditions, the orientational interaction in Eq. (2) can generate a sufficiently large ω_m to activate the threshold condition in Eq. (3) for both robots and resulting in stable chiral motion. We numerically compute the probability for four robots ($N = 4$) to reach chiral phase from random conditions, P_4 . Figure S8 shows that P_4 is close to unity in the majority of the parameter regime to the right of the boundary lines defined by Eq. (4). This indicates that an increase in N and the inclusion of intraspecies interaction result in a greater variety of initial configurations, from which all robots converge toward the threshold Ω to form chiral states.

With insights from the few-robot models, we now embark on a comprehensive investigation of the 48-robot system in Fig. 1. We numerically construct a phase diagram of different states, which is shown in Fig. 3(a), with experimental data plotted as symbols. The diagram is divided by white boundary lines, defined in Eq. (4), into two regions. Time-invariant flocking and antiflocking states and time-dependent chiral states appear in the left and right regions, respectively. With parameters close to the boundary lines, the system may randomly switch between different states; we label this region as mixed [43].

In time-invariant flocking and antiflocking states, robot angular velocity is generally small enough that the threshold mechanism in Eq. (3) seldom comes into play. As a result, these states in our work are similar to their counterparts in Ref. [33]. However, chiral states in two systems exhibit distinct differences. In Ref. [33], both the angular velocity and heading difference change with interaction

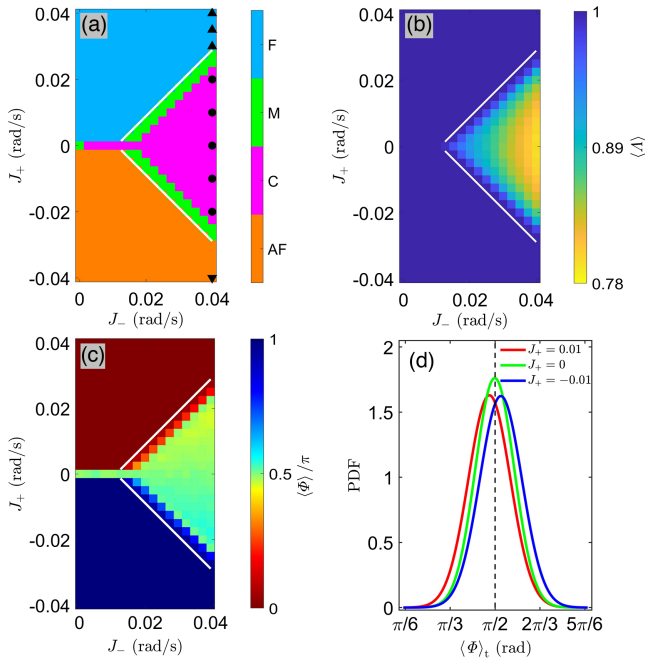


FIG. 3. Collective states of 48 interacting robots. (a) Phase diagram from numerical simulations, showcasing different states: flocking (F), mixed (M), chiral (C), and antiflocking (AF) states. Experimental data points are represented as symbols: circles, upper triangles, and lower triangles correspond to chiral, flocking, and antiflocking states, respectively. (b) Mean polar order parameter within species. (c) Mean heading difference between the two species. (d) Probability distributions of heading difference from random initial conditions at three different parameter sets with $J_- = 0.04$ rad/s, $J_+ = 0.01, 0, -0.01$ rad/s. Results in (b)–(d) are obtained from simulations. The parameters used include $J_{AA} = J_{BB} = 0.0175$ rad/s, $\Omega = 0.267$ rad/s, and $v_0 = 10$ mm/s. Simulations are conducted with periodic boundary conditions, without local repulsive interaction and without random noises. The white lines in (a)–(c) are defined by Eq. (4).

parameters. In our system, robots in chiral states maintain identical angular velocities of Ω or $-\Omega$ (Fig. S21) and the mean heading difference is approximately $\pi/2 \pm 0.24$ rad [Figs. 3(c) and 3(d)]. Within each species, robots exhibit significant polar order [Fig. 3(b)]. This results in weak intraspecies orientational interactions. Consequently, interspecies interactions dominate the orientation dynamics outlined in Eq. (2). This observation leads to a simple picture that the heading dynamics in chiral states approximately resemble those of the two-robot model with effective interaction constants of $(N/2)J_{AB}$ and $(N/2)J_{BA}$ [41]. This clarifies why stable chiral states in Fig. 3(a) are only attainable with parameter values situated to the right of the boundary equation Eq. (4). We systematically change various parameters, including Ω , N , noise level, interaction constants, robot and boundary repulsion, and boundary conditions. Through these parameter variations, we consistently observe the emergence of phase

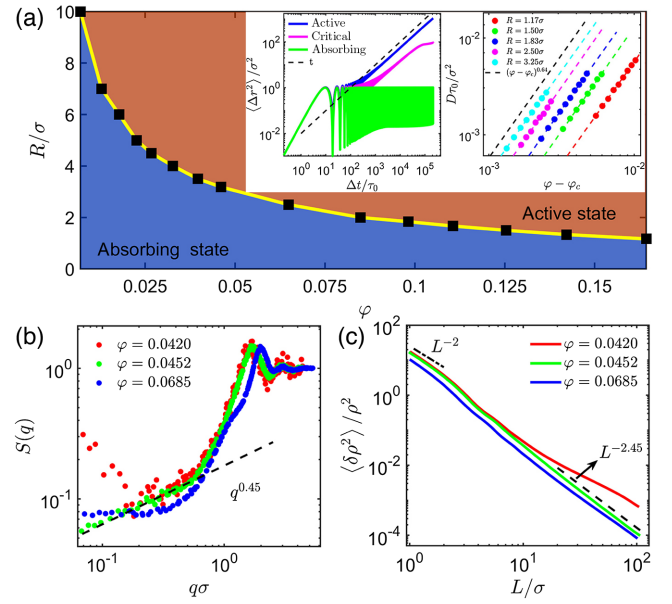


FIG. 4. Absorbing-active transition and density fluctuation in chiral states from simulations. (a) Dynamic phase diagram of $N = 2048$ robots plotted in the plane of area fraction φ and local repulsion range R (main panel). Inset on the left: mean-squared displacements with $R = 1.83\sigma$ at three different area fractions (blue, $\varphi = 0.0997$; magenta, $\varphi = 0.0994$; green, $\varphi = 0.0905$); also see Movie S6 [43]. Inset on the right: diffusion constant D as functions of φ for different R . (b) Static structure factors and (c) density fluctuations computed with $R = 3.25\sigma$, at three densities with $N = 8192$ and $W = 23\,500, 22\,628$ and $18\,390$ mm. Parameters include: $J_+ = 0.005$ rad/s, $J_- = 0.04$ rad/s, $J_{AA} = J_{BB} = 0.035$ rad/s, $v_0 = 10$ mm/s, and $\Omega = 0.33$ rad/s.

diagrams akin to that in Fig. 3(a). As detailed in Sec. IV(F) in the SM [43], Ω and N control the positions of the boundary lines, whereas other parameter variations primarily influence the states in proximity to these boundary lines.

In results presented so far, we have taken deliberate measures to mitigate the influence of robot-robot repulsion to facilitate the comparison with the Vicsek model. For example, the local repulsion in Fig. 1 is constrained to a limited range $R = 260$ mm. Consequently, 48 robots in Fig. 1(d) enter an absorbing state, characterized by robot separations exceeding R , wherein they execute localized circular motion with a diameter $\sigma = 2v_0/\Omega$. However, if a large R is used, as shown in Movies S4 and S5 [43], robots can robustly form chiral states but they are persistently repelled by their neighbors, entering an active state. We systematically investigate the absorbing-active transition in simulations, featuring N robots confined within a periodic box with a width W . In absorbing states with small area fraction $\varphi = \pi N \sigma^2 / 4W^2$ or R , mean-squared displacements of the robots exhibit a plateau over long time, as illustrated in the left inset of Fig. 4(a). In contrast, active states exhibit diffusive translational motion with particle

diffusivity D , which is used to pinpoint the critical condition for the transition. For a given repulsion range R , the diffusivity data in the right inset of Fig. 4(a) exhibit power-law scaling: $D \sim (\varphi - \varphi_c)^\beta$ with $\beta \approx 0.64$, close to the exponent associated with the conserved directed percolation universality class [52]. The extracted critical area fraction φ_c are plotted in Fig. 4(a) to define the phase boundary.

We measure density fluctuations near the transition. Static structure factors in Fig. 4(b) reveal a scaling $S(q) \sim q^{0.45}$ for small q and density fluctuations in (c) scale with the measurement window size as $\langle \delta\rho^2 \rangle \sim L^{-2.45}$ for large L at φ_c ; $S(q)$ measured in states away from the transition deviate from the $q^{0.45}$ scaling. These data show that, at the transition, robots organize themselves in a hyperuniform state with suppressed density fluctuations [53–63]. Hyperuniformity with the same scaling exponent is robustly observed with other parameter settings; see Sec. V(B) in the SM [43]. The scaling exponent for $S(q)$, 0.45, agrees with that in a variety of systems [55,62,63]. Although our experimental system of 48 robots is too limited in scale to directly demonstrate hyperuniformity, we can still use the system to explore the effects of robot-robot repulsion. In particular, we run experiments with a set of parameters ($R = 8.83\sigma$ and $\varphi = 0.01$) in close proximity to the phase boundary in Fig. 4(a). The results in Movie S5 and Fig. S22 [43] affirm that local repulsion drives the robots to disperse uniformly, which significantly reduces density fluctuations.

We have implemented an experimental system comprising programmable robots to explore the NR collective dynamics [33,41]. Our system introduces two previously unconsidered factors: angular speed threshold and local repulsion. The threshold proves instrumental in stabilizing chiral states arising from the NR interactions. We elucidated the underlying stabilization mechanism and identified the essential working conditions through analytical and numerical models. Additionally, our numerical simulations have demonstrated that robots within the chiral states undergo an absorbing-active transition as local repulsion strength increases and that disordered hyperuniform states emerge at the transition. These findings demonstrate the versatility of nonreciprocity and its fusion with other physical effects as a strategy for generating time-dependent collective states with diverse and intriguing properties.

We thank Xiaqing Shi, Yongfeng Zhao, Mingji Huang, Hugues Chate, and Masaki Sano for helpful discussions. We acknowledge support from the National Natural Science Foundation of China (Grants No. 12225410, No. 12074243, and No. 62076203), the Fundamental Research Funds for the Central Universities and the Student Innovation Center at Shanghai Jiao Tong University.

*xiaokanglei@xauat.edu.cn

†pxg@nwpu.edu.cn

‡hepeng_zhang@sjtu.edu.cn

- [1] J. N. Israelachvili, *Intermolecular and Surface Forces* (Elsevier, Amsterdam, 1992).
- [2] A. V. Ivlev, J. Bartnick, M. Heinen, C. R. Du, V. Nosenko, and H. Loewen, *Phys. Rev. X* **5**, 011035 (2015).
- [3] A. Poncet and D. Bartolo, *Phys. Rev. Lett.* **128**, 048002 (2022).
- [4] M. C. Marchetti, J. F. Joanny, S. Ramaswamy, T. B. Liverpool, J. Prost, M. Rao, and R. A. Simha, *Rev. Mod. Phys.* **85**, 1143 (2013).
- [5] C. Bechinger, R. Di Leonardo, H. Löwen, C. Reichhardt, G. Volpe, and Giovanni Volpe, *Rev. Mod. Phys.* **88**, 045006 (2016).
- [6] G. Gompper *et al.*, *J. Phys. Condens. Matter* **32**, 193001 (2020).
- [7] M. J. Bowick, N. Fakhri, M. C. Marchetti, and S. Ramaswamy, *Phys. Rev. X* **12**, 010501 (2022).
- [8] Q. S. Chen, A. Patelli, H. Chate, Y. Q. Ma, and X. Q. Shi, *Phys. Rev. E* **96**, 020601(R) (2017).
- [9] S. Saha, S. Ramaswamy, and R. Golestanian, *New J. Phys.* **21**, 063006 (2019).
- [10] L. P. Dadhichi, J. Kethapelli, R. Chajwa, S. Ramaswamy, and A. Maitra, *Phys. Rev. E* **101**, 052601 (2020).
- [11] R. K. Gupta, R. Kant, H. Soni, A. K. Sood, and S. Ramaswamy, *Phys. Rev. E* **105**, 064602 (2022).
- [12] M. Knezevic, T. Welker, and H. Stark, *Sci. Rep.* **12**, 19437 (2022).
- [13] K. L. Kreienkamp and S. H. L. Klapp, *New J. Phys.* **24** (2022).
- [14] E. Theveneau, B. Steventon, E. Scarpa, S. Garcia, X. Trepac, A. Streit, and R. Mayor, *Nat. Cell Biol.* **15**, 763 (2013).
- [15] A. I. Curatolo, N. Zhou, Y. Zhao, C. Liu, A. Daerr, J. Tailleur, and J. Huang, *Nat. Phys.* **16**, 1152 (2020).
- [16] R. Niu, T. Palberg, and T. Speck, *Phys. Rev. Lett.* **119**, 028001 (2017).
- [17] T. Yu, P. Chuphal, S. Thakur, S. Y. Reigh, D. P. Singh, and P. Fischer, *Chem. Commun. (Cambridge)* **54**, 11933 (2018).
- [18] F. Schmidt, B. Liebchen, H. Loewen, and G. Volpe, *J. Chem. Phys.* **150**, 094905 (2019).
- [19] C. H. Meredith, P. G. Moerman, J. Groenewold, Y.-J. Chiu, W. K. Kegel, A. van Blaaderen, and L. D. Zarzar, *Nat. Chem.* **12**, 1136 (2020).
- [20] C. Wu, J. Dai, X. Li, L. Gao, J. Wang, J. Liu, J. Zheng, X. Zhan, J. Chen, X. Cheng, M. Yang, and J. Tang, *Nat. Nanotechnol.* **16**, 288 (2021).
- [21] G. Gardi and M. Sitti, *Phys. Rev. Lett.* **131**, 058301 (2023).
- [22] M. Brandenbourger, X. Locsin, E. Lerner, and C. Coulais, *Nat. Commun.* **10**, 4608 (2019).
- [23] F. A. Lavergne, H. Wendehenne, T. Bauerle, and C. Bechinger, *Science* **364**, 70 (2019).
- [24] G. Wang, T. V. Phan, Trung, S. Li, M. Wombacher, J. Qu, Y. Peng, G. Chen, D. I. Goldman, Daniel, S. A. Levin, R. H. Austin, and L. Liu, *Phys. Rev. Lett.* **126**, 108002 (2021).
- [25] H. Massana-Cid, C. Maggi, G. Frangipane, and R. Di Leonardo, *Nat. Commun.* **13**, 2740 (2022).
- [26] X. Wang, P.-C. Chen, K. Kroy, V. Holubec, and F. Cichos, *Nat. Commun.* **14**, 56 (2023).

- [27] M. Y. B. Zion, J. Fersula, N. Bredeche, and O. Dauchot, *Sci. Robot.* **8**, eabo6140 (2023).
- [28] S. Saha, J. Agudo-Canalejo, and R. Golestanian, *Phys. Rev. X* **10**, 041009 (2020).
- [29] Z. You, A. Baskaran, and M. C. Marchetti, *Proc. Natl. Acad. Sci. U.S.A.* **117**, 19767 (2020).
- [30] T. Frohoff-Huelsmann, J. Wrembel, and U. Thiele, *Phys. Rev. E* **103**, 042602 (2021).
- [31] R. Mandal, S. S. Jaramillo, and P. Sollich, *arXiv*: 2212.05618.
- [32] F. Brauns and M. C. Marchetti, *arXiv*:2306.08868.
- [33] M. Fruchart, R. Hanai, P. B. Littlewood, and V. Vitelli, *Nature (London)* **592**, 363 (2021).
- [34] J. Agudo-Canalejo and R. Golestanian, *Phys. Rev. Lett.* **123**, 018101 (2019).
- [35] D. Martin, D. Seara, Y. Avni, M. Fruchart, and V. Vitelli, *arXiv*:2307.08251.
- [36] Y. Duan, J. Agudo-Canalejo, R. Golestanian, and B. Mahault, *Phys. Rev. Lett.* **131**, 148301 (2023).
- [37] Y. J. Chiu and A. K. Omar, *J. Chem. Phys.* **158**, 164903 (2023).
- [38] T. Vicsek, A. Czirok, E. Benjacob, I. Cohen, and O. Shochet, *Phys. Rev. Lett.* **75**, 1226 (1995).
- [39] H. Chate, *Annu. Rev. Condens. Matter Phys.* **11**, 189 (2020).
- [40] S. Chatterjee, M. Mangeat, C. U. Woo, H. Rieger, and J. D. Noh, *Phys. Rev. E* **107**, 024607 (2023).
- [41] R. Hanai, *Phys. Rev. X* **14**, 011029 (2024).
- [42] R. El-Ganainy, K. G. Makris, M. Khajavikhan, Z. H. Musslimani, S. Rotter, and D. N. Christodoulides, *Nat. Phys.* **14**, 11 (2018).
- [43] See Supplemental Material at <http://link.aps.org/supplemental/10.1103/PhysRevLett.132.118301> for detailed experimental and numerical results, and movies from experiments and simulations.
- [44] O. Chepizhko and F. Peruani, *Phys. Rev. Lett.* **111**, 160604 (2013).
- [45] C. W. Reynolds, *SIGGRAPH Comput. Graph.* **21**, 25 (1987).
- [46] I. D. Couzin, J. Krause, R. James, G. D. Ruxton, and N. R. Franks, *J. Theor. Biol.* **218**, 1 (2002).
- [47] G. Vasarhelyi, C. Viragh, G. Somorjai, T. Nepusz, A. E. Eiben, and T. Vicsek, *Sci. Robot.* **3**, eaat3536 (2018).
- [48] A. Deblais, T. Barois, T. Guerin, P. H. Delville, R. Vaudaine, J. S. Lintuvuori, J. F. Boudet, J. C. Baret, and H. Kellay, *Phys. Rev. Lett.* **120**, 188002 (2018).
- [49] T. Barois, J.-F. Boudet, J. S. Lintuvuori, and H. Kellay, *Phys. Rev. Lett.* **125**, 238003 (2020).
- [50] Q. Yang, H. W. Zhu, P. Liu, R. Liu, Q. F. Shi, K. Chen, N. Zheng, F. F. Ye, and M. C. Yang, *Phys. Rev. Lett.* **126**, 198001 (2021).
- [51] Y. Kuramoto, *Chemical Oscillations, Waves, and Turbulence*, Dover Books on Chemistry Series (Dover Publications, New York, 2003).
- [52] M. Henkel, H. Hinrichsen, and S. Lubeck, *Non-Equilibrium Phase Transitions. Volume 1: Absorbing Phase Transitions* (Springer, New York, 2009), Vol. 2008.
- [53] S. Torquato and F. H. Stillinger, *Phys. Rev. E* **68**, 041113 (2003).
- [54] S. Torquato, *Phys. Rep.* **745**, 1 (2018).
- [55] E. Tjhung and L. Berthier, *Phys. Rev. Lett.* **114**, 148301 (2015).
- [56] J. H. Weijs, R. Jeanneret, R. Dreyfus, and D. Bartolo, *Phys. Rev. Lett.* **115**, 108301 (2015).
- [57] J. Wang, J. M. Schwarz, and J. D. Paulsen, *Nat. Commun.* **9**, 2836 (2018).
- [58] Q.-L. Lei, M. P. Ciamarra, and R. Ni, *Sci. Adv.* **5**, eaau7423 (2019).
- [59] M. J. Huang, W. S. Hu, S. Y. Yang, Q. X. Liu, and H. P. Zhang, *Proc. Natl. Acad. Sci. U.S.A.* **118**, e2100493118 (2021).
- [60] B. Zhang and A. Snezhko, *Phys. Rev. Lett.* **128**, 218002 (2022).
- [61] N. Oppenheimer, D. B. Stein, M. Y. Ben Zion, and M. J. Shelley, *Nat. Commun.* **13**, 804 (2022).
- [62] D. Hexner and D. Levine, *Phys. Rev. Lett.* **114**, 110602 (2015).
- [63] D. Hexner, P. M. Chaikin, and D. Levine, *Proc. Natl. Acad. Sci. U.S.A.* **114**, 4294 (2017).